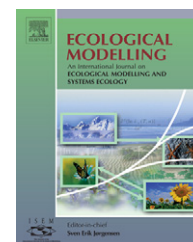


available at www.sciencedirect.comjournal homepage: www.elsevier.com/locate/ecolmodel

On the use of the advanced very high resolution radiometer for development of prognostic land surface phenology models

Naven Kathuroju^a, Michael A. White^{a,*}, Jürgen Symanzik^b, Mark D. Schwartz^c, James A. Powell^b, Ramakrishna R. Nemani^d

^a Department of Watershed Sciences, Utah State University, Logan, UT, USA

^b Department of Mathematics and Statistics, Utah State University, Logan, UT, USA

^c Department of Geography, University of Wisconsin-Milwaukee, Milwaukee, WI, USA

^d NASA Ames Research Center, Moffett Field, CA, USA

ARTICLE INFO

Article history:

Received 24 November 2005

Received in revised form

17 August 2006

Accepted 5 September 2006

Published on line 18 October 2006

Keywords:

Budburst

Climate change

Senescence

Leaf out

Growing season

Interannual variability

Spring

Fall

Canopy duration

Carbon

GCM

ABSTRACT

Regulation of interannual phenological variability is an important component of climate and ecological models. Prior phenological efforts using the advanced very high resolution radiometer (AVHRR) as a proxy of vegetation dynamics have often simulated spring events only or failed to simulate interannual variability. Our aim is to address these shortcomings and to use the AVHRR to develop prognostic models for interannual land surface phenology and, critically, to test whether or not the developed models are superior to use of climatological phenology values from the AVHRR. Using datasets for the conterminous United States, we first filtered data to select regions and plant functional types for which the best-possible remotely sensed signal could be obtained. We then used a generalized linear model approach to model the relationship between an integrative productivity index and estimates of the start of season (SOS) and end of season (EOS) derived from the AVHRR, yielding models capable of prognostically predicting SOS/EOS events independently of satellite data. Mean absolute errors between the model-predicted and AVHRR-observed SOS/EOS ranged from 5.1 to 20.3 days. SOS errors were uniformly lower than EOS errors. SOS models for the deciduous broadleaf forest and grassland plant functional types produced lower errors than use of the climatological SOS values while all other models produced errors higher than those obtained from the climatological dates. Based on this criterion for success, we suggest that the AVHRR may not be appropriate for further development of prognostic land surface phenology models. However, an intercomparison of phenological dates from an independent spring index model, our model predictions, and the AVHRR observations indicated that interannual predictions from our models may be superior to the satellite data upon which they are based, implying that a further comparison between models based on the AVHRR and newer, superior sensors, should be conducted.

© 2006 Elsevier B.V. All rights reserved.

* Corresponding author.

E-mail address: mikew@cc.usu.edu (M.A. White).

0304-3800/\$ – see front matter © 2006 Elsevier B.V. All rights reserved.

doi:10.1016/j.ecolmodel.2006.09.011

1. Introduction

Phenology, the study of the timing of recurring biological cycles and their connection to climate, is a critical field in global change science (Penuelas and Filella, 2001; Menzel, 2002). For terrestrial ecosystem and climate models, vegetation phenology is important in at least three central areas. First, although interannual variation in canopy duration is not a primary determinant of annual carbon fluxes (White and Nemani, 2003), failure to incorporate realistic phenological subroutines will induce serious errors in simulated carbon fluxes (up to 20% errors across the normal range of phenological variability; White et al., 1999). Second, energy balance calculations, as influenced by the partitioning of net radiation into latent and sensible heat, are strongly influenced by phenological variability in climate models (Levis and Bonan, 2004). Third, for the emerging field of hydrologic forecasting (e.g. <http://ecocast.arc.nasa.gov/>), accurate prediction of phenological variability is especially important for areas characterized by low levels of canopy cover (White and Nemani, 2004). Phenology is also a crucial component of land–atmosphere interactions (Schwartz, 1992; Fitzjarrald et al., 2001), evapotranspiration (Guillevic et al., 2002), patterns of soil organic matter (Epstein et al., 1999), and the seasonality of carbon fluxes (Baldocchi et al., 2001). The importance and utility of phenology, while widely recognized in a broad modeling community (e.g. Lu and Shuttleworth, 2002), has not led to extensive efforts to develop prognostic phenology models compatible with coarse resolution ecological and climate models. Indeed, this shortcoming has been identified specifically as a major need for future modeling efforts (Kucharik et al., 2006). Here, we attempt to address this need by expanding on prior attempts to develop prognostic phenology models.

Climate and coarse resolution ecosystem models typically simulate plant functional types, not individual species. Species-specific phenology models, which may or may not be representative of general landscape phenology, are therefore inappropriate. For large-area modeling efforts, satellite remote sensing observations of land surface phenology are in practice the only proxy of vegetation seasonality obtained at an appropriate level of aggregation. The satellite signal, representing the phenological integration of the entire pixel, is termed land surface phenology (de Beurs and Henebry, 2004a) and includes the usually undesirable confounding effects of soil, snow, and atmospheric variability.

For late 20th century and current periods, satellite datasets may be used directly to monitor land surface phenology (Justice et al., 1985; Lloyd, 1990; Reed et al., 1994; Myneni et al., 1997a; Duchemin et al., 1999; Chen et al., 2000; Zhang et al., 2004) and to force directly vegetation seasonality in climate and/or ecological models. However, many modeling applications involve simulations for periods prior to the satellite record and/or for future climate scenarios. In these cases, remote sensing cannot be used to regulate vegetation seasonality: prognostic land surface phenology models are necessary.

Such models, in which the timing of a specific event such as the start of season (SOS) or end of season (EOS) is predicted, are comparatively rare. Botta et al. (2000) extrapolated

land surface phenology models valid over a regional scale to a global scale and developed models to determine the time of leaf onset. White et al. (1997) developed land surface phenology models to determine the SOS and EOS for grassland and deciduous broad leaf forest (DBF) plant functional types in the conterminous United States. Kaduk and Heimann (1996) used simulations of net primary production and climate dependent plant physiological rules to simulate land surface phenology.

These and other studies often contain one or more limitations: (1) regions with mixed plant functional types are used, introducing multiple phenological signals that may respond differently to interannual climate variability; (2) mean land surface phenology events are predicted, not interannual phenological variability (Botta et al., 2000; Arora and Boer, 2005); (3) satellite data are not screened to remove less than ideal conditions; (4) *a priori* assumptions are made about the environmental factors controlling the timing of land surface phenology events; (5) only spring models are developed; (6) a single arbitrary stage of canopy development is selected as a phenological event; (7) model prediction errors are not compared to use of the mean (climatological) phenological date as the prediction.

Here, our goal was to address all seven limitations and to test whether or not the advanced very high resolution radiometer (AVHRR), the sensor with longest continuous record of high frequency global observations of land surface phenology, can be used to develop rigorous prognostic land surface phenology models for use in ecological and/or climate models. To our knowledge, no similar effort has investigated whether or not such models can predict interannual phenological variability with errors lower than those obtained when simply using climatological phenology.

2. Data

We conducted our analysis for the conterminous United States from 1990 to 1997 (1994 excepted due to satellite failure). Model development required meteorology and remote sensing datasets. All data were produced at or resampled and reprojected to a 1 km resolution in the Lambert's Azimuthal Equal Area projection.

2.1. Meteorology

We obtained 1990–1997 one-kilometer daily meteorology for the conterminous United States from the DAYMET dataset (Thornton et al., 1997). The data, interpolated from weather station records, include maximum temperature, minimum temperature, precipitation, shortwave radiation, and vapor pressure deficit.

2.2. Remote sensing

We obtained three remotely sensed datasets. First, we obtained 14-day composited (Holben, 1986) 1 km AVHRR normalized difference vegetation index (NDVI) data from the Earth Resources Observations & Science Data Center (EDC). We then calculated leaf area index (LAI) using NDVI and the algorithms in Myneni et al. (1997b). We retained the EDC-assigned

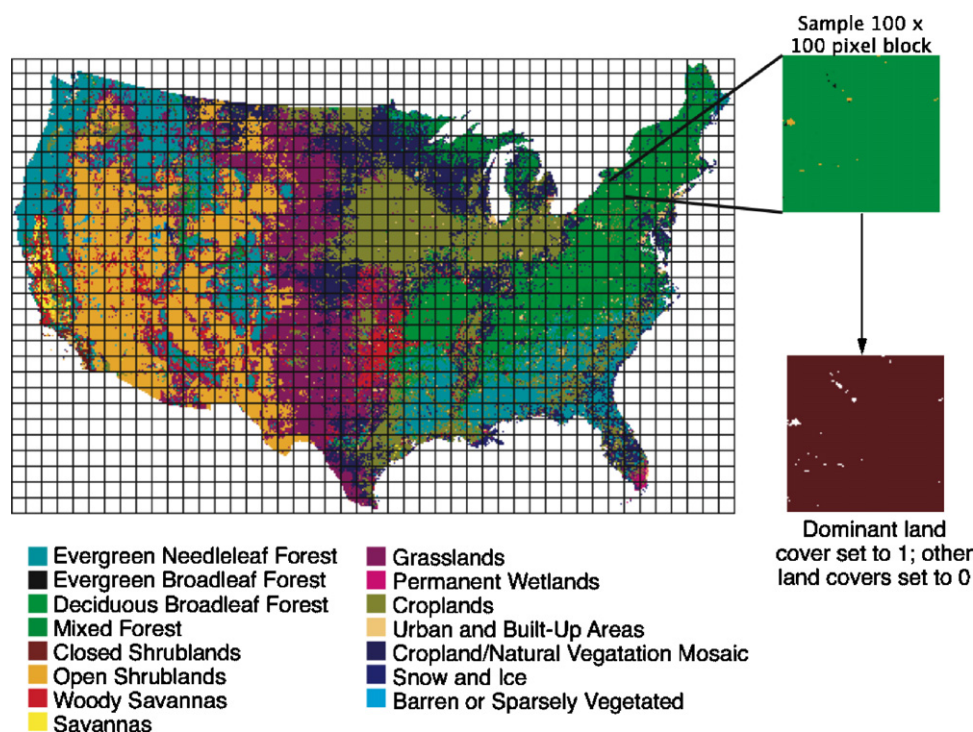


Fig. 1 – Initial study region based on plant functional type. Superimposed grid shows the 100 × 100 pixel block layout. The single expanded DBF block shows the creation of the binary mask containing 1 for the dominant plant functional type and 0 for other pixels. All analysis was conducted on pixels of the dominant plant functional type only.

date of maximum NDVI for each pixel in each 14-day composited period and used this date information in subsequent spatial compositing (Appendix A). Second, we obtained plant functional type data based on categorical (Fig. 1, Hansen et al., 2000) and continuous fields classifications (containing percent herbaceous and tree cover information; Hansen et al. (2003), used in Appendix B). Third, we used the 1982–1999 wavelet dataset in White et al. (2005) showing, for all pixels, the number of years in which the wavelet power spectrum was highest at the annual time scale (data used in Appendix B). A higher number of years indicated a clear, detectable, and consistent annual NDVI cycle.

2.3. Ground data

As this research relies heavily on estimates of interannual variability derived from satellites, an assessment of these estimates is highly desirable. Yet validation and/or interpretation of land surface phenology remote sensing is, at best, exceedingly difficult. Most ground-based observations are made at single points. Due to the extreme spatial discontinuity between a single plant(s) and pixel(s) and the inherent within-stand variability of ground phenological processes, such ground data should not be used for validation of coarse resolution satellite data. The best compromise may be to compare a spatially distributed proxy measurement of ground phenology to satellite phenology estimates: we implemented this approach with the Spring Indices (SI) First Bloom model (Schwartz et al., 2002) driven by inputs from the 1990

to 1997 DAYMET dataset to simulate the First Bloom stage (most related to native species leaf phenology; Schwartz et al., 2002) at a 1 km resolution for the conterminous United States. The SI First Bloom model, developed as a composite indicator of spring phenological variability for clonal honeysuckle (*Lonicera tatarica*, *L. korolkowii*) and lilac (*Syringa chinensis*) has been extensively validated (Schwartz, 2003) and is considered to be an excellent proxy for ground measurements.

3. Methods

3.1. Site selection

Following the policy advocated in White et al. (2005), we focused our test on regions representing best-possible conditions for AVHRR remote sensing and model development. To minimize problems with satellite issues like cloud contamination, pixel misregistration, and the low signal to noise ratio of the AVHRR sensor, we first divided the landscape into 100 × 100 pixel regions, termed blocks (10,000 km², Fig. 1). We selected the 100 × 100 size as a compromise designed to minimize the potential of crossing major climatic zones while still providing sufficient numbers of pixels for spatial compositing. We then implemented a sequential filtering process to select blocks representing pure plant functional types and to remove blocks unfavorable for remote sensing and/or modeling (Appendix B).

3.2. Time variant model inputs

For each block, we generated, as described below, 7 years of data (1990–1997, 1994 excepted) for the response (LAI) and explanatory (productivity index) variables used in model development. A complete annual sequence of time variant data at a single 100×100 block is termed a block-year. Our goal here was to use spatial compositing to produce a single daily LAI curve and a single daily productivity index curve characterizing the seasonal dynamics of each block-year.

3.2.1. LAI and observed SOS/EOS

Snow, cloud, and other atmospheric contamination caused extremely noisy LAI profiles, even for 14-day composites. For prognostic land surface phenology models, since the goal is to relate the seasonal progression of some measure of “greenness”, such as NDVI or LAI, to some measure of environmental conditions, preprocessing is required to minimize LAI variability unrelated to vegetation phenology. We developed daily LAI curves for each block-year by conducting outlier removal, spatial compositing, upper envelope fitting, interpolation, and smoothing (Appendix A).

Predictions of canopy development relative to regional LAI patterns, not to absolute LAI value, are usually desired for prognostic phenology schemes. We therefore scaled each LAI block-year curve between 0 and 1 (details in Appendix A). We defined SOS (EOS) as the yearday when the scaled LAI exceeded (passed below) a specified percent of annual maximum scaled LAI (referred to as canopy stages). We developed separate models for 20%, 30%, and 40% canopy stages; results were very similar and we present below only results for SOS and EOS at the 20% canopy stage. See Appendix A for an example of SOS/EOS processing.

3.2.2. Productivity index

Some land surface modeling schemes have assumed *a priori* the mechanism(s) controlling canopy development whereas use of a single variable representing an integration of multiple potentially limiting factors is preferable (Jolly et al., 2005). Here, we adopted this concept through a productivity index based on the Biome-BGC daily carbon assimilation routines (White et al., 2000; Thornton et al., 2002) (Fig. 2). We used a constant unit LAI for all calculations. The productivity index, although expressed in units of gCm^{-2} , is not meant to represent a biophysical process and should not be considered to be a true simulated carbon flux. Rather, it is used to simultaneously incorporate the main radiation, temperature, and moisture factors known to limit plant growth (Fig. 2).

For each pixel of the dominant plant functional type we initialized soil water content at saturation, conducted a 7-year spinup, simulated the 7-year period with soil water content initialized from the spinup, and created a daily productivity index curve for each block-year by averaging the productivity index on each yearday. Because grasslands are sensitive to soil water stress (Pitt and Wikeem, 1990) and use of a unit LAI may underestimate summer water stress, we performed parallel simulations to calculate the soil water potential scalar using the remotely sensed LAI and incorporated this in estimating the grassland productivity index.

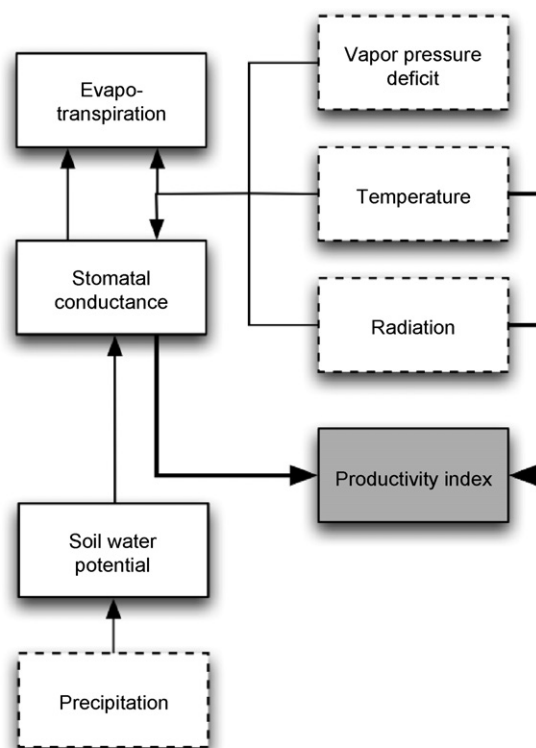


Fig. 2 – Schematic of productivity index simulations. Vapor pressure deficit, temperature, incident radiation, and precipitation inputs from DAYMET (Thornton et al., 1997) shown with dashed boxes. Stomatal conductance is calculated with a Jarvis approach (Jarvis, 1976) and is affected by scalars for soil water potential, vapor pressure deficit, temperature, and radiation. Soil water potential is calculated (Clapp and Hornberger, 1978) from soil water content derived from soil properties (White and Nemani, 2004), precipitation inputs, and outputs (Penman–Monteith evapotranspiration (Monteith, 1995) plus runoff). The productivity index (shaded box) is simulated using the Farquhar photosynthesis model (Farquhar et al., 1980), which is affected by temperature controls on enzyme activity, incident solar radiation, and intercellular CO_2 concentration (a function of stomatal conductance; Ball et al., 1987). See Thornton (1998) for further details. Variables with a direct control over the productivity index are shown as thick lines; other feedbacks are indirect.

3.3. Modeling the relationship between productivity index and SOS/EOS

3.3.1. Defining critical summations

Based on extensive research in the phenological literature, SOS is highly related to summations of favorable environmental conditions, often growing degree days (de Beurs and Henebry, 2004a). Once the critical summation is reached, SOS or a similar event is predicted to occur. Here, we used the productivity index as the basis for our summations. We assessed a large range of starting days and productivity index thresholds (value above which productivity index is used towards the summation) and found that model results were insensi-

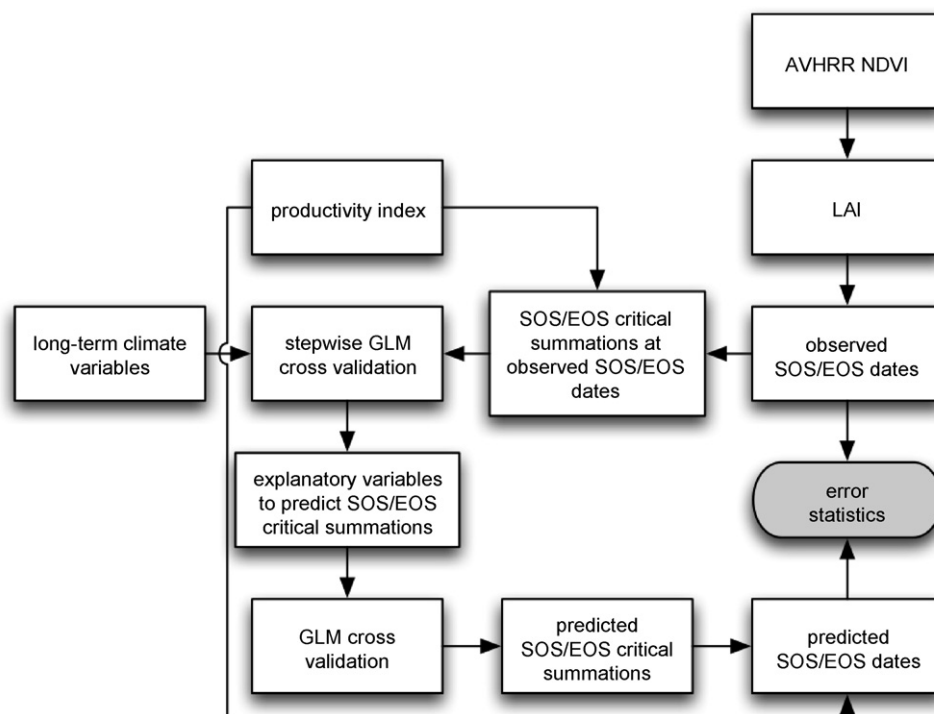


Fig. 3 – Schematic of modeling process.

tive to these parameterizations. Therefore we calculated the cumulative summation of productivity index values from 1 January to the satellite-observed SOS for all plant functional types and all block-years (Fig. 3). We termed these values SOS critical summations.

For the fall phenology model, a transformation of the productivity index was required such that low values, associated with unfavorable environmental conditions, would be magnified. We again assessed a large range of transformations and found that $1/\text{productivity index}^{1/2}$ produced best results. We calculated summations of the transformed productivity index from SOS to EOS and termed these values EOS critical summations.

3.3.2. SOS and EOS predictions

We observed clear spatial variations in SOS/EOS critical summations within plant functional types such that warmer regions usually required larger summations; use of a single critical summation within plant functional types would have introduced extensive regional biases. We were therefore mandated to model SOS/EOS critical summations prior to generating predictions of SOS and EOS. Note that we implemented the following modeling process to represent the use of prognostic land surface phenology schemes in climate change scenarios; use of critical summations corresponding to contemporary remote sensing estimates of SOS/EOS would lead to progressive biases under changing climates.

We first identified variables useful for predicting SOS/EOS critical summations (Fig. 3). Exploratory analysis suggested that long-term climate variables were related to the spatial variability of critical summations. We thus used a suite of

block-averaged DAYMET climatic metrics as possible explanatory variables: averages of 1990–1997 daily mean temperature ($^{\circ}\text{C}$) and precipitation (cm) and spring (March, April, May), summer (June, July, August), fall (September, October, November), and winter (December, January, February) averages of 1990–1997 daily maximum temperature, minimum temperature, and precipitation. We included annual total potential evapotranspiration and annual water deficit from White et al. (2003) and average block latitude.

We used an automated forward stepwise generalized linear model (log link function, S-PLUS, Version 6.2.1 for Sun SPARC, SunOS 5.8, Insightful Corp.) coupled with a 10-fold cross-validation (Stone, 1974) to select variables useful for the prediction of SOS/EOS critical summations (Fig. 3). At each iteration of the 10-fold cross-validation, we used the stepwise procedure to identify, individually and in combination, the climate variables in the development group (90% of block-years) producing a best fit for the spatial variation of observed SOS/EOS critical summations in the validation group (10% of block-years). We used this process to identify, for each plant functional type, the explanatory variables occurring in at least 50% of the stepwise procedures, not to actually predict SOS/EOS critical summations.

Using these commonly occurring explanatory variables, we then implemented a second 10-fold cross-validation procedure coupled with the generalized linear model (stepwise process now eliminated) to predict SOS/EOS critical summations and, based on these summations, SOS/EOS dates (Fig. 3). In each cross-validation iteration, we used the development blocks to model SOS/EOS critical summations for the validation blocks. We calculated predicted SOS (EOS) as the yearday

when summations of the productivity index (transformed productivity index) exceeded the SOS (EOS) critical summation. We term this approach, based on the generalized linear models, to be the prognostic date model.

Differences between the prognostic date model SOS/EOS and observed SOS/EOS (from scaled AVHRR LAI) generated differences in days. We calculated the mean absolute error and bias for each plant functional type. We used a one-sided t-test to test whether or not the grassland prognostic date model with the productivity index soil water scalar derived from actual LAI was superior to prognostic date models using the unit LAI.

3.3.3. Comparison to SI simulations

We extracted predicted and observed SOS dates at the 20% canopy stage (conceptually closest to SI First Bloom dates) for all DBF blocks existing at or above the lower latitude limit of station data used to develop the SI models ($\sim 38^\circ\text{N}$). For the same blocks, and only for DBF pixels (SI models not comparable to ENF, grasslands, or croplands), we calculated block average SI First Bloom dates. We calculated and compared: the range and standard deviation at each block; the North to South gradient of 1990–1997 means at each block; and the relationship between interannual anomalies at each block.

3.3.4. Comparing to the climatological model

We termed a prognostic date model to be successful if it produced lower mean absolute errors than models using climatological AVHRR-derived SOS/EOS dates as the predictor. For this test, we calculated the mean 1990–1997 observed SOS/EOS yearday for each block, used these values as the prediction for each block-year, and generated mean absolute error values. We termed this the mean date model.

4. Results

4.1. Block selection

After implementing removal of block-years with LAI outliers (Appendix A) and the block filtering process (Appendix B), there were 280 block-years in the DBF, 171 in evergreen needle-leaf forest (ENF), 469 in cropland, and 288 in grassland. Other plant functional types were removed in the filtering process (Appendix B).

4.2. Critical summations

Variables used by the generalized linear model to predict critical summations varied strongly by plant functional type (Table 1). DBF SOS critical summations were a function of annual temperature alone while for other plant functional types at least two explanatory variables were used. Other critical summations were simulated by the following: latitude and fall temperature and precipitation in DBF EOS; seasonal temperature or potential evapotranspiration in ENF; winter temperatures or moisture-related variables in grasslands; and a highly diverse assemblage of variables in croplands (Table 1). S-PLUS objects for the final models are available (Kathuroju, 2005).

4.3. Model performance

The success of prognostic date models developed through the cross-validation approach varied widely. Mean absolute error ranged from a low of 5.1 days for DBF SOS to a high of 20.3 days for grassland EOS (Table 2). Bias was less than 2 days for six out of eight models but was 4.5 days for grassland EOS. In terms

Table 1 – Explanatory variables used to predict the spatial variation of SOS and EOS critical summations at 20% of annual maximum scaled LAI

	SOS critical summation	EOS critical summation
DBF	Temperature	Fall maximum temperature Fall precipitation Latitude
ENF	Spring maximum temperature Summer maximum temperature	Potential evapotranspiration Summer minimum temperature
Grasslands	Fall precipitation Water deficit Winter maximum temperature Winter minimum temperature	Summer precipitation Water deficit
Croplands	Fall maximum temperature Potential evapotranspiration Spring precipitation Summer maximum temperature summer precipitation Water deficit Winter maximum temperature Winter precipitation Fall maximum temperature	Fall maximum temperature Potential evapotranspiration Spring precipitation Summer precipitation Summer maximum temperature Water deficit Winter maximum temperature Winter minimum temperature Winter precipitation

The selected variables appeared in at least half of the cross-validation iterations.

Table 2 – Errors statistics from prognostic date models and comparison to mean date models (Δ is the difference between prognostic date model and mean date model in mean absolute error; negative values indicate that the prognostic date model produced superior results)

	Bias	Mean absolute error	r^2	Δ
SOS				
DBF	0.5	5.1	0.7	–0.1
ENF	1.5	9.6	0.3	1.1
Grasslands	1.3	8.6	0.3	–0.7
Croplands	0.7	7.3	0.8	0.8
EOS				
DBF	0.4	6.0	0.1	2.1
ENF	2.3	11.4	0.1	1.5
Grasslands	4.5	20.3	0.0	7.0
Croplands	1.0	7.6	0.5	1.8

of mean absolute error and r^2 , SOS models were superior to EOS models for all plant functional types (Table 2). SOS predictions were usually close to the 1:1 line but grassland and ENF SOS models demonstrated overprediction for early observed SOS and underprediction for late observed SOS (Fig. 4). For EOS, three central findings existed (Fig. 4): (1) the range of EOS dates was much lower in DBF and ENF than in the non-woody plant functional types; (2) results for the extremely variable observed grassland EOS (approximately 140-day range) were highly scattered along the 1:1 line; (3) cropland EOS models were tightly clustered along the 1:1 and appeared to capture the range of observed EOS well.

Grassland prognostic date models in which the soil water scalar for stomatal conductance was forced by water fluxes based on actual LAI (as opposed to unit LAI as for other simulations) did not produce improved models (paired difference t-tests P-values from 0.25 to 0.5 for SOS). For the EOS models, in which we expected an improved measure of drought stress to improve model results, the minor improvements in bias and mean absolute error were not statistically significant (P-values from 0.05 to 0.25).

4.4. Comparisons to SI dates

There were 31 DBF blocks available for comparisons of SI First Bloom dates, observed SOS (from AVHRR LAI), and predicted SOS (from prognostic date models). Across blocks, the average range between the earliest and latest dates was: 16.3 days for SI, 18.5 days for observed SOS, and 14.6 days for predicted SOS. The average standard deviations were: 5.8 days for SI, 6.4 days for observed SOS, and 5.6 days for predicted SOS. When the 1990–1997 average dates were calculated for each block (i.e. one average date per block) and expressed as an anomaly versus the mean across all 31 blocks, the SI dates showed an almost doubled North to South gradient (43 days) than either the predicted or observed SOS dates (24 days), with SI earlier than SOS in the South and later in the North. Based on averages of 31 individual block r^2 values, interannual anomalies were highly correlated between SI and predicted SOS (average $r^2 = 0.85$, all values greater than 0.6) and less so between SI and observed SOS (average $r^2 = 0.7$, nine values less than 0.6). Sim-

ilarly, interannual anomalies were statistically related at the 5% level (F-test) for 29 of 31 SI versus predicted SOS comparisons but for only 18 of 31 SI versus observed SOS comparisons.

4.5. Testing against the climatological model

The prognostic date models outperformed the mean date model for DBF and grassland SOS predictions (Table 2). Otherwise, the mean date model produced lower mean absolute error. Relative to the mean date model, the performance of the prognostic date model was worse for EOS predictions than for SOS predictions in all plant functional types.

5. Discussion

5.1. Data selection and development

With our goal of pursuing model development only in those regions best suited to produce a clear LAI signal for pure plant functional types, removal of most of the conterminous United States as possible study regions was inevitable. Similarly, White et al. (2005) found that most terrestrial pixels were unsuitable for long-term global phenological monitoring. Given the many known liabilities of the AVHRR sensor (Gutman et al., 1994; de Beurs and Henebry, 2004b) and other liabilities related to landscape fragmentation, atmospheric contamination, and variation in soil background, we submit that our approach was appropriate. Further, since our main goal was to test whether or not the AVHRR could be used to develop rigorous prognostic land surface phenology models, not to develop models representing the synoptic coverage of plant functional types, this elimination was acceptable.

5.2. Explanatory variables for critical summations

While the generalized linear model is an empirical approach, the variables selected to predict SOS/EOS critical summations varied by plant functional type and may be related to underlying factors controlling phenological variability. In woody plant functional types, temperature and energy availability variables dominated model variables whereas precipitation occurred only once (Table 1). Photoperiod, as represented by the latitude proxy, was important for DBF, suggesting a strong non-biotic control of EOS phenology. On the other hand, moisture related variables dominated predictions of grassland critical summations, especially for EOS. Numerous predictors, probably corresponding to a large range of crop types and farming practices, controlled cropland SOS and EOS critical summations.

5.3. Model performance

In spite of our extensive efforts to: (1) conduct remote sensing and modeling in regions with pure and homogeneous plant functional types; (2) identify strong phenological signals; (3) rigorously screen and process LAI data; (4) employ an integrative productivity index, the prognostic date model was no better than use of the mean date model for six out of eight models. We also developed models in which we predicted

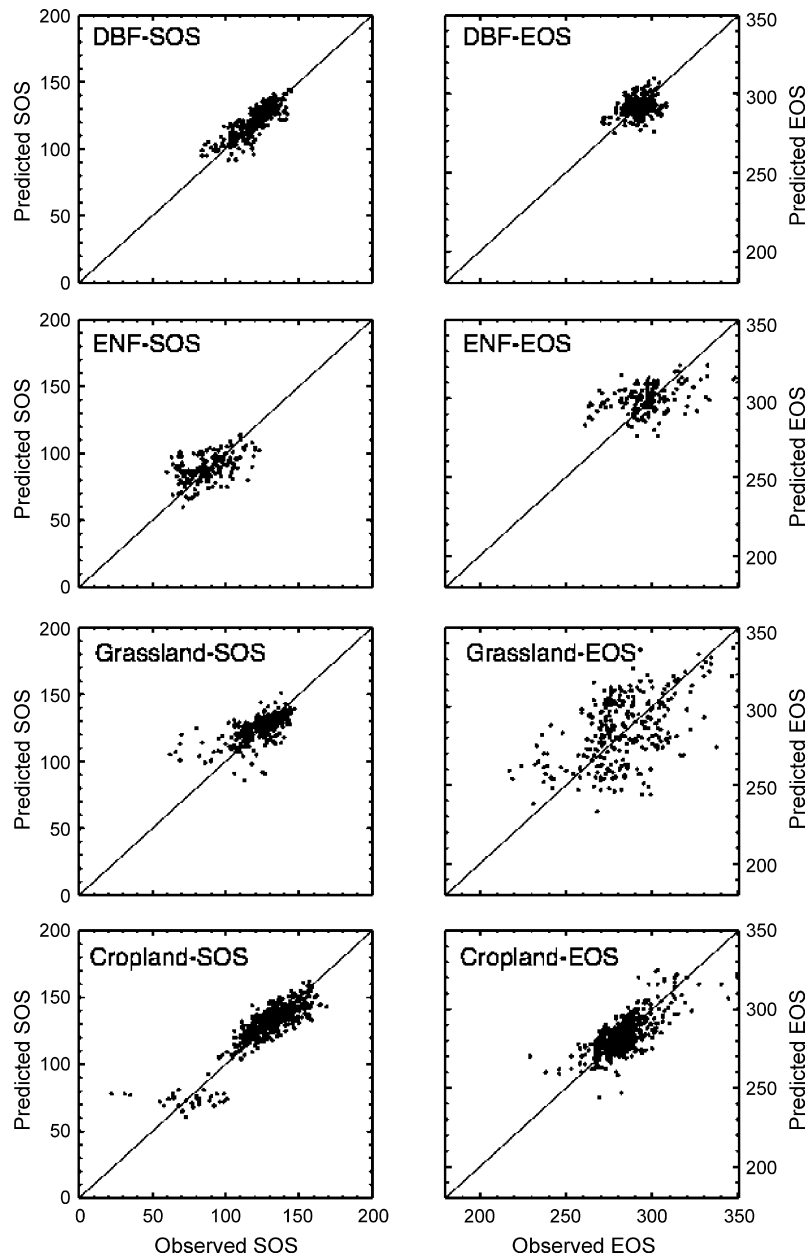


Fig. 4 – Predicted vs. observed SOS and EOS. Each point represents a block-year. 1:1 line shown for comparison. Refer to Table 2 for error statistics.

residuals from the mean date, as opposed to the date itself, and models in which we predicted only early, average, and late events. These efforts were no more successful than the approaches outlined above and are not presented.

Spring events in DBF and grasslands, as suggested by low mean absolute error (Table 2), represent tractable phenomena for modeling and remote sensing. Winter LAI is near zero and increases rapidly in the spring. DBF, with a higher peak LAI than most grassland blocks, represents the ideal case for remote sensing of vegetation phenology. In all other cases, biological and/or technical problems may have limited the accuracy of the observed SOS/EOS training data. In DBF, EOS had a limited range strongly associated with photoperiod (Table 1 and Fig. 4). Remote sensing of grassland observed EOS was

especially problematic, as senescence patterns in most blocks were characterized by stepped patterns of LAI drops followed by plateaus of variable length. In these cases, small variations in LAI at the plateaus altered observed EOS by several weeks. Variable snow cover patterns and limited LAI seasonality likely influenced observed ENF SOS and EOS. Crop phenology is at least partially controlled by variables such as planting times, fertilization, and irrigation, none of which were represented in productivity index simulations.

While these findings may seem to indicate a limited utility for this modeling approach, our comparison of SI First Bloom dates versus predicted and observed SOS suggests an alternate interpretation. The SI dates, which are highly related to both the original lilac and honeysuckle development data

and to clonal species in the European Phenological Gardens (Schwartz et al., 2006), are an excellent proxy indicator of interannual variability and trends in ground phenology. When averaged across sites, predicted and observed SOS showed very similar range and standard deviation to SI First Bloom. Examined along the North to South gradient, though, SI First Bloom showed a greater dynamic range. Given that the SI model is tuned to clonal species and uses constant critical summations, it is likely that SI dates are systematically different than actual ground vegetation (earlier in the South and later in the North). Schwartz (1992) discussed this pattern (differential environmental adaptation), and gave a similar estimate of the effect's impact (14 days greater range) across the same study region. Thus, absolute value comparisons between SI First Bloom and satellite must account for this effect; we therefore now focus only on comparing interannual variability.

In this context, while interannual anomalies of both observed and predicted SOS dates had strong relationships with SI First Bloom, predicted SOS was more strongly correlated to SI and had more frequent statistically significant relationships. This finding suggests that models developed from satellite estimates of land surface phenology paradoxically may be more related to actual vegetation phenology than the satellite data itself. In essence, it is possible that the observed SOS dates provide an approximation of mean and interannual variability for the DBF but that prognostic date models using environmental conditions (productivity index), are a more reliable metric of phenological variability. As this phenomenon seems to exist for remote sensing in the best-case DBF, we speculate that this same pattern may exist, but to an even greater extent, for other PFTs, and that our results may understate model performance.

6. Conclusion

We developed prognostic land surface phenology models to predict the interannual variability of AVHRR-observed SOS/EOS dates and found that, except for SOS in DBF and grasslands, use of AVHRR climatological SOS/EOS dates as the predictor variable produced superior results. We do not imply that all sensors will produce similar results or that the overall approach is without merit. To address whether or not technical sensor problems, lack of ancillary snow and atmospheric data, and/or structural errors in our productivity index approach and meteorological drivers are responsible for model difficulties, the above procedure should be replicated using data from the much-improved MODIS sensor.

Our central conclusion is that while the AVHRR sensor presents challenges for further research on interannual prognostic phenology, modeling the interannual variability of spring phenology for DBF and grasslands is highly tractable. Given that (1) these plant functional types, separately and in combination (as savannas), are extensively distributed and (2) climate change is occurring mostly in spring and our approach flexibly adapts to climate change, our results will be applicable in many situations. For other biomes, we advocate a strategy in which species-specific models or observations are coupled with remotely sensed climatological dates. In this scheme, remote sensing would be used to represent patterns of mean

land surface phenology while ground-based processes independent of remote sensing (e.g. the planned National Phenology Network, <http://www.uwm.edu/Dept/Geography/npn/>) would regulate interannual variability.

Appendix A. Generation of daily LAI curves and identification of SOS/EOS

A plot of LAI information from all the pixels in a sample block-year is shown in Fig. A.1. As we retained the yearday at which each pixel was selected for each composite period, many more than the expected 26 dates (14 days per composite period = 26 composite periods expected per year) are available. Two themes are apparent, as they are for nearly all block-years: (1) there is a clear upper envelope and (2) the profile is extremely noisy. Our goal was to fit a daily LAI curve to the upper envelope of values without selecting high outliers. We assumed that this profile would best represent true vegetation development and that low LAI values represented some measure of signal contamination. The six-step process was as follows. First, we used a logistic regression filter to eliminate high outliers and to select the remaining high LAI values:

1.1 Obtain the distribution of LAI on a given day (step 1, Fig. A.1).

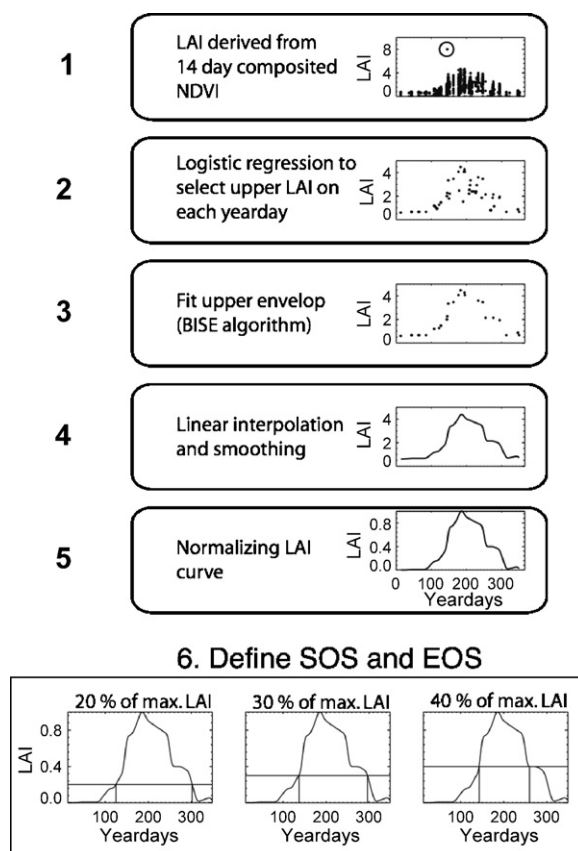


Fig. A.1 – LAI processing scheme. Circled value in step 1 is a high outlier removed by the logistic regression process. For each bottom panel at each percent threshold (horizontal line), left vertical line shows SOS and right vertical line shows EOS.

- 1.2 Sort the LAI values and calculate a cumulative summation of the distribution.
- 1.3 Scale the cumulative summation between 0 and 1.
- 1.4 Perform the logistic transformation on the scaled data (Eq. (A.1)). Transformation of the highest LAI value (scaled to 1 in step 3) is undefined and is removed here.

$$p^* = \log\left(\frac{p}{1-p}\right) \quad (\text{A.1})$$

- 1.5 Fit a polynomial to the remaining values. If the number of values is greater than or equal to 3 and less than or equal to 5 then fit a third order polynomial. If the number of values is greater than 5 then fit a fifth order polynomial. If fewer than three values are available, discard all data and proceed to the next day.
- 1.6 Perform an inverse transformation on the fitted values (y) using Eq. (A.2).

$$p = \frac{e^y}{1 + e^y} \quad (\text{A.2})$$

- 1.7 Extract the LAI value(s) corresponding to the 95th to 99th percentiles on the scaled cumulative summation. From this range, retain the highest LAI value. If there are no LAI values within this range, extract the highest value (step 2, Fig. A.1).

For some block-years, clear outliers still remained, usually in late winter or early fall when a spike in LAI was followed by a return to lower values before the usual seasonal canopy expansion began. Thus, in our second step, we manually eliminated obvious high outliers (required for 13% of the grassland block-years, 11% of DBF block-years, 23% of ENF block-years, and 4% of cropland block-years). Note that we removed only those block-years with clearly aberrant seasonal profiles. Third, as frequent low LAI values still existed, we fitted an LAI envelope using the Best Index Slope Extraction method (Viovy and Arino, 1992) (step 3, Fig. A.1). In Best Index Slope Extraction, extremely large LAI increases and short-term LAI drops are ignored while large and persistent LAI decreases are accepted. Fourth, we linearly interpolated the resultant upper envelope to obtain daily LAI values and then smoothed the data with a 7-day window (step 4, Fig. A.1). Fifth, despite our efforts in selection and processing, a limited number of block-years still contained extremely spurious LAI curves. As our ultimate goal is to develop prognostic models, not to produce estimates of phenological events for every possible case, we eliminated the block-years with spurious LAI curves (6 grassland block-years and 39 ENF block-years in ENF). Sixth, as the EDC AVHRR NDVI data are known to contain within and among sensor calibration problems (Schwartz et al., 2002), we normalized the LAI curves (White et al., 1997) of all the block-years (step 5, Fig. A.1):

$$\text{scaled LAI} = \frac{\text{LAI} - \text{LAI}_{\min}}{\text{LAI}_{\max} - \text{LAI}_{\min}} \quad (\text{A.3})$$

where LAI_{\min} is the median of the lowest 30 LAI values and LAI_{\max} is the maximum annual LAI. We obtained LAI_{\min} as the median of lowest 30 LAI values in a year to eliminate any

bias in the normalized LAI curve that might be caused due to a persisting low outlier and reset all LAI values below LAI_{\min} to LAI_{\min} . This approach obviates problems potentially arising from drift in the absolute magnitude of the NDVI values used to produce LAI.

Once the scaled LAI profile was developed for each block-year, we extracted SOS and EOS (step 6, Fig. A.1). SOS occurred when the scaled LAI exceeded the specified canopy stage threshold (20, 30, or 40% of annual maximum LAI); EOS occurred when the scaled LAI fell below the specified canopy stage threshold. To test the sensitivity of SOS/EOS dates to processing approach, we assessed phenological metrics from a global 8 km AVHRR dataset (Pinzon et al., 2005) using three methods: (1) relative thresholds annual, as here; (2) absolute thresholds defined as the midpoint between long-term average minimum and maximum values; (3) a derivative-based approach. Interannual variability and trends in SOS and EOS from the three approaches were highly related (not shown, contact corresponding author for details); therefore our SOS and EOS dates are unlikely to be highly sensitive to the processing method.

Appendix B. Block filtering

Given the initial distribution of 100×100 pixel blocks (Fig. 1), the block filtering process consisted of the following six steps (Fig. B.1).

1. Screen blocks by plant functional type. Eliminate evergreen broad leaf forest, urban, and wetland plant functional types due to sparse coverage and shrublands due to low seasonal and interannual LAI variability. Based on multiple and potentially confounding phenological signals present within mixed plant functional types, eliminate savanna, cropland/natural vegetation mosaic, and mixed forest plant functional types. Remaining blocks are deciduous broad leaf forest (DBF), and evergreen needle leaf forest (ENF), grassland, or cropland.
2. For these four plant functional types, eliminate blocks with less than 10% cover and accept blocks with greater than 50% cover by the dominant plant functional type. Fig. B.1a shows block distribution to this point.
3. For remaining blocks, set pixels of the dominant plant functional type to 1 and all other pixels to 0 (see Fig. 1 for example). Use metrics based on Moran's I (Moran, 1948), a measure of connectivity between a pixel and its adjacent pixels, to eliminate non-homogeneous blocks, which would represent highly dispersed landscapes prone to problems of misregistration and/or plant functional type misclassification. Moran's I is

$$I = \frac{n \sum_{i=1}^n \sum_{j=1}^n w_{ij} (x_i - \bar{x})(x_j - \bar{x})}{\left(\sum_{i=1}^n \sum_{j=1}^n w_{ij} \right) \left(\sum_{i=1}^n (x_i - \bar{x})^2 \right)} \quad (\text{B.1})$$

where I = Moran's I , n = number of pixels, w_{ij} = weight (here a Euclidean distance) between a reference pixel (i) and another pixel (j), x_i = the value contained by the reference pixel (i), x_j = the value contained by the other pixel (j) in an

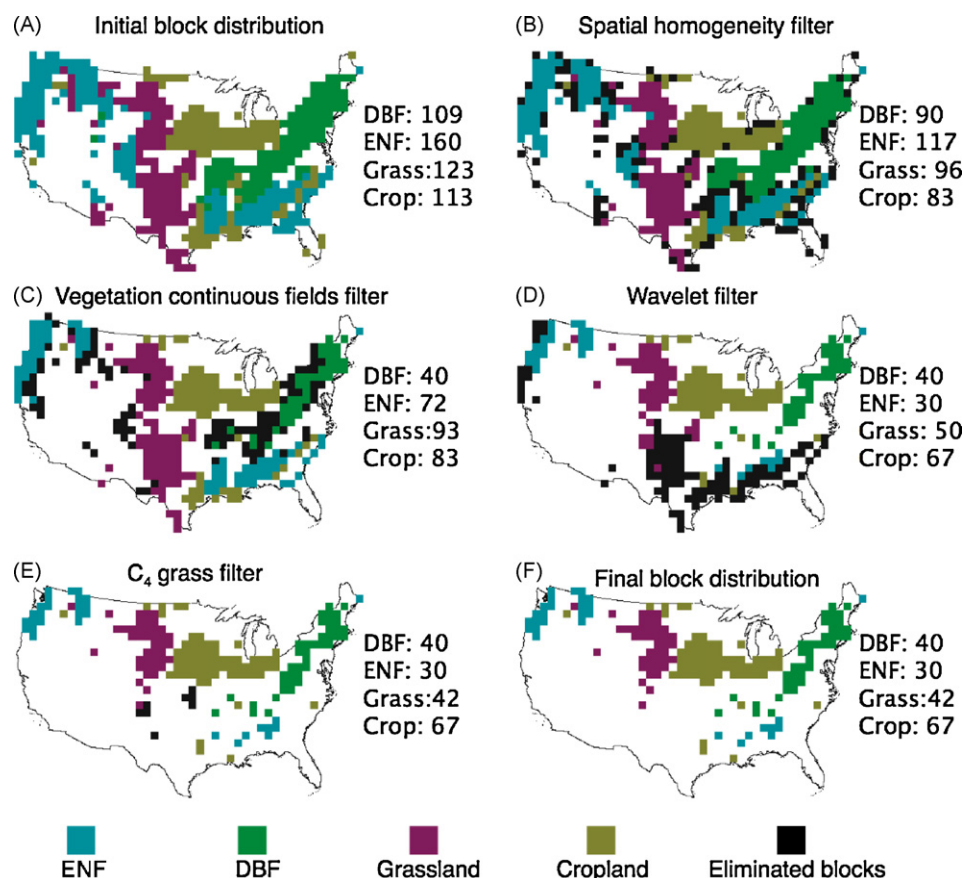


Fig. B.1 – Block filtering process. The initial distribution included all blocks with greater than 10% cover by one of the pure plant functional types. Blocks were removed by filters for spatial homogeneity, vegetation continuous fields, wavelet seasonality, and presence of C₄ grasses, leading to the final block distribution. Figure text shows the number of blocks available after each filter.

image, and \bar{x} is the mean of all pixel values. Moran's I does not have a fixed range but is typically between -1 (strong negative spatial homogeneity) and 1 (strong positive spatial homogeneity). Implement as follows:

- 3.1 Assume that only blocks representing a landscape composed of 10 or fewer "clumps" of the dominant plant functional type would be selected (allowing blocks with more than 10 clumps removed few blocks while a stricter rule eliminated extensive study regions).
- 3.2 Use a cellular automata approach to develop the statistical distribution of Moran's I for hypothetical 100×100 pixel landscape blocks with 10, 20, 30, 40, and 50% cover by the dominant plant functional: initialize all pixels to 0 and then randomly assign 10 pixels (corresponding to 10 clumps) to 1; for each pixel set to 1, randomly assign one of the eight neighbors to 1; iterate until the desired percent cover of 1s is reached (10, 20, 30, 40, or 50%); calculate Moran's I ; repeat process 1000 times; from this distribution identify the 5th percentile as a cutoff value (Moran's I values of 0.69 at 10%; 0.76 at 20%; 0.79 at 30%; 0.80 at 40%, 0.81 at 50%).
- 3.3 For each 100×100 pixel block (Fig. 1), calculate the percent cover by the dominant plant functional type and calculate Moran's I ; if this value is greater than or equal to the cutoff value of the closest theoretical distribution, the block passes the spatial homogeneity filter (Fig. B.1b).
4. Filter with the vegetation continuous fields data to eliminate blocks unrepresentative of pure plant functional types. Calculate the average herbaceous or tree percent cover for all pixels in a block corresponding to the dominant vegetation type and eliminate cropland and grassland blocks with less than 50% herbaceous cover and DBF and ENF blocks with less than 50% tree cover (Fig. B.1c).
5. Filter with the wavelet dataset by assuming that analysis should be conducted only in those regions where the annual NDVI cycle is consistently strong. Calculate, for the pixels representing the dominant plant functional type, the average number of years in which the strongest wavelet power occurred at the annual scale (out of a possible 17) and eliminate all blocks for which the mean number of years was less than 14 (Fig. B.1d).
6. Distribution of C₄ grasslands, found in areas with long-term annual average temperature greater than 10°C (Sims, 1988), was extremely sparse and unlikely to produce robust models. Therefore eliminate C₄ grassland blocks (Fig. B.1e). Final block distribution shown in Fig. B.1f.

REFERENCES

- Arora, V.K., Boer, G.J., 2005. A parameterization of leaf phenology for the terrestrial ecosystem component of climate models. *Glob. Change Biol.* 11, 39–59.
- Baldocchi, D., Falge, E., Wilson, K., 2001. A spectral analysis of biosphere–atmosphere trace gas flux densities and meteorological variables across hour to multi-year time scales. *Agric. For. Meteorol.* 107, 1–27.
- Ball, J., Woodrow, I., Berry, J., 1987. A model predicting stomatal conductance and its contribution to the control of photosynthesis under different environmental conditions. In: Biggins, I. (Ed.), *A model predicting stomatal conductance and its contribution to the control of photosynthesis under different environmental conditions*. Progress in Photosynthetic Research. Martinus Nijhoff Publishers, Netherlands, pp. 221–224.
- Botta, A., Viovy, N., Ciais, P., Friedlingstein, P., Monfray, P., 2000. A global prognostic scheme of leaf onset using satellite data. *Glob. Change Biol.* 6, 709–726.
- Chen, X., Tan, Z., Schwartz, M.D., Xu, C., 2000. Determining the growing season of land vegetation on the basis of plant phenology and satellite data in Northern China. *Int. J. Biometeorol.* 44, 97–101.
- Clapp, R.B., Hornberger, G.M., 1978. Empirical equations for some soil hydraulic properties. *Water Resour. Res.* 14, 601–604.
- de Beurs, K.M., Henebry, G.M., 2004a. Land surface phenology, climatic variation, and institutional change: analyzing agricultural land cover change in Kazakhstan. *Remote Sens. Environ.* 89, 497–509.
- de Beurs, K.M., Henebry, G.M., 2004b. Trend analysis of the Pathfinder AVHRR Land (PAL) NDVI data for the deserts of Central Asia. *IEEE Geosci. Remote Sens. Lett.* 1, 282–286.
- Duchemin, B., Goubier, J., Courrier, G., 1999. Monitoring phenological key stages and cycle duration of temperate deciduous forest ecosystems with NOAA/AVHRR data. *Remote Sens. Environ.* 67, 68–82.
- Epstein, H.E., Burke, I.C., Lauenroth, W.K., 1999. Response of the shortgrass steppe to changes in rainfall seasonality. *Ecosystems* 2, 139–150.
- Farquhar, G.D., von Caemmere, S., Berry, J.A., 1980. A biochemical model of photosynthetic CO₂ assimilation in leaves of C₃ species. *Planta* 149, 78–90.
- Fitzjarrald, D.R., Acevedo, O.C., Moore, K.E., 2001. Climatic consequences of leaf presence in the eastern United States. *J. Clim.* 14, 598–614.
- Guillevic, P., Koster, R.D., Suarez, M.J., Bounoua, L., Collatz, G.J., Los, S.O., Mahanama, S.P.P., 2002. Influence of the interannual variability of vegetation on the surface energy balance—a global sensitivity study. *J. Hydrometeorol.* 3, 617–629.
- Gutman, G.G., Ignatov, A.M., Olson, S., 1994. Towards better quality of AVHRR composite images over land: reduction in cloud contamination. *Remote Sens. Environ.* 50, 134–148.
- Hansen, M.C., DeFries, R., Townshend, J., Carroll, M., Dimiceli, C., Sohlberg, R., 2003. Global percent tree cover at a spatial resolution of 500 meters: first results of the MODIS vegetation continuous fields algorithm. *Earth Interactions*, 7:Paper No. 10.
- Hansen, M.C., DeFries, R.S., Townshend, J.R.G., Sohlberg, R., 2000. Global land cover classification at 1 km resolution using a decision tree classifier. *Int. J. Remote Sens.* 21, 1331–1365.
- Holben, B.N., 1986. Characteristics of the maximum-value composite images from temporal AVHRR data. *Int. J. Remote Sens.* 7, 1417–1434.
- Jarvis, P.G., 1976. The interpretation of the variations in leaf water potential and stomatal conductance found in canopies in the field. *Phil. Trans. Roy. Soc. London, Ser. B* 273, 593–610.
- Jolly, W.M., Nemani, R., Running, S.W., 2005. A generalized, bioclimatic index to predict foliar phenology in response to climate. *Glob. Change Biol.* 11, 619–632.
- Justice, C.O., Townshend, J.R.G., Holben, B.N., Tucker, C.J., 1985. Analysis of the phenology of global vegetation using meteorological satellite data. *Int. J. Remote Sens.* 6, 1271–1318.
- Kaduk, J., Heimann, M., 1996. A prognostic phenology model for global terrestrial carbon cycle models. *Clim. Res.* 6, 1–19.
- Kathuroju, N., 2005. Coarse resolution vegetation phenology modeling. M.S. Thesis. Utah State University, Logan.
- Kucharik, C.J., Barford, C.C., El Maayar, M., Wofsy, S.C., Monson, R.K., Baldocchi, D.D., 2006. A multiyear evaluation of a Dynamic Global Vegetation Model at three AmeriFlux forest sites: vegetation structure, phenology, soil temperature, and CO₂ and H₂O vapor exchange. *Ecol. Modell.* 196, 1–31.
- Levis, S., Bonan, G.B., 2004. Simulating springtime temperature patterns in the community atmosphere model coupled to the community land model using prognostic leaf area. *J. Clim.* 17, 4531–4540.
- Lloyd, D., 1990. A phenological classification of terrestrial vegetation cover using shortwave vegetation index imagery. *Int. J. Remote Sens.* 11, 2269–2279.
- Lu, L.X., Shuttleworth, W.J., 2002. Incorporating NDVI-derived LAI into the climate version of RAMS and its impact on regional climate. *J. Hydrometeorol.* 3, 347–362.
- Menzel, A., 2002. Phenology, its importance to the global change community. *Clim. Change* 54, 379–385.
- Monteith, J.L., 1995. A reinterpretation of stomatal responses to humidity. *Plant Cell Environ.* 18, 357–364.
- Moran, P., 1948. The interpretation of statistical maps. *J. Roy. Stat. Soc., Ser. B* 10, 243–251.
- Myneni, R.B., Keeling, C.D., Tucker, C.J., Asrar, G., Nemani, R.R., 1997a. Increased plant growth in the northern high latitudes from 1981 to 1991. *Nature* 386, 698–702.
- Myneni, R.B., Nemani, R.R., Running, S.W., 1997b. Estimation of global leaf area index and absorbed PAR using radiative transfer models. *IEEE Trans. Geosci. Remote Sens.* 35, 1380–1393.
- Penuelas, J., Filella, I., 2001. Phenology—responses to a warming world. *Science* 294, 793–795.
- Pinzon, J., Brown, M.E., Tucker, C.J., 2005. EMD correction of orbital drift artifacts in satellite data stream. In: Huang, N., Shen, S. (Eds.), *EMD correction of orbital drift artifacts in satellite data stream*. The Hilbert-Huang Transform and its Applications. World Scientific Publishing Co, Hackensack, NJ, pp. 167–183.
- Pitt, M.D., Wikeem, B.M., 1990. Phenological patterns and adaptations in an *Artemisia/Agropyron* plant community. *J. Range Manage.* 43, 350–367.
- Reed, B.C., Brown, J.F., VanderZee, D., Loveland, T.R., Merchant, J.W., Ohlen, D.O., 1994. Measuring phenological variability from satellite imagery. *J. Veg. Sci.* 5, 703–714.
- Schwartz, M.D., 1992. Phenology and springtime surface-layer change. *Monthly Weather Rev.* 120, 2570–2578.
- Schwartz, M.D., 2003. Phenoclimatic measures. In: Schwartz, M. (Ed.), *Phenoclimatic measures*. Phenology: An Integrative Environmental Science. Kluwer Academic Publishers, New York, NY, pp. 331–343.
- Schwartz, M.D., Ahas, R., Aasa, A., 2006. Onset of spring starting earlier across the northern hemisphere. *Glob. Change Biol.* 12, 343–351.
- Schwartz, M.D., Reed, B., White, M.A., 2002. Assessing satellite-derived start-of-season (SOS) measures in the conterminous USA. *Int. J. Climatol.* 22, 1793–1805.
- Sims, P.L., 1988. Grasslands. In: Barbour, M.G., Billings, W.D. (Eds.), *Grasslands*. North American Terrestrial Vegetation. Cambridge University Press, pp. 265–286.
- Stone, M., 1974. Cross-validatory choice and assessment of statistical predictions. *J. Roy. Stat. Soc., Ser. B* 36, 111–133.

- Thornton, P.E., 1998. Regional ecosystem simulation: combining surface- and satellite-based observations to study linkages between terrestrial energy and mass budgets. Ph.D. Dissertation. University of Montana, Missoula, MT.
- Thornton, P.E., Law, B.E., Gholz, H.L., Clark, K.L., Falge, E., Ellsworth, D.S., Goldstein, A.H., Monson, R.K., Hollinger, D., Paw, U., Chen, J., Sparks, J., 2002. Modeling and measuring the effects of disturbance history and climate on carbon and water budgets in evergreen needleleaf forests. *Agric. For. Meteorol.* 113, 185–222.
- Thornton, P.E., Running, S.W., White, M.A., 1997. Generating surfaces of daily meteorological variables over large regions of complex terrain. *J. Hydrol.* 190, 214–251.
- Viovy, N., Arino, O., 1992. The best index slope extraction (BISE): a method for reducing noise in NDVI time-series. *Int. J. Remote Sens.* 13, 1585–1590.
- White, M.A., Brunsell, N., Schwartz, M.D., 2003. Vegetation phenology in global change studies. In: Schwartz, M.D. (Ed.), *Vegetation phenology in global change studies. Phenology: An Integrative Environmental Science*. Kluwer Academic Publishers, New York, NY, pp. 453–466.
- White, M.A., Hoffman, F., Hargrove, W.W., Nemani, R.R., 2005. A global framework for monitoring phenological responses to climate change. *Geophys. Res. Lett.* 32, L0475, doi:10.1029/2004GL021961.
- White, M.A., Nemani, R.R., 2003. Canopy duration has little effect on annual carbon storage in the eastern United States broad leaf forest. *Glob. Change Biol.* 9, 972–976.
- White, M.A., Nemani, R.R., 2004. Soil water forecasting in the continental United States: relative forcing by meteorology versus leaf area index and the effects of meteorological forecast errors. *Can. J. Remote Sens.* 30, 717–730.
- White, M.A., Running, S.W., Thornton, P.E., 1999. The impact of growing-season length variability on carbon assimilation and evapotranspiration over 88 years in the eastern U.S. deciduous forest. *Int. J. Biometeorol.* 42, 139–145.
- White, M.A., Thornton, P.E., Running, S.W., 1997. A continental phenology model for monitoring vegetation responses to interannual climatic variability. *Glob. Biogeochem. Cycles* 11, 217–234.
- White, M.A., Thornton, P.E., Running, S.W., Nemani, R.R., 2000. Parameterization and sensitivity analysis of the BIOME-BGC terrestrial ecosystem model: net primary production controls. *Earth Interact.* 4, 1–85.
- Zhang, X.Y., Friedl, M.A., Schaaf, C.B., Strahler, A.H., Schneider, A., 2004. The footprint of urban climates on vegetation phenology. *Geophys. Res. Lett.* 31, L12209, doi:10.1029/2004GL020137.